Experimental and numerical investigation on a passive control system for the mitigation of vibrations on SDOF and MDOF structures: mini Tribological ROCKing Seismic Isolation Device

L. Giresini[a]*, M.L. Puppio[a], F. Laccone[a,b] and M. Froli[a]

[a] *Department of Energy, Systems, Territory and Construction Engineering, University of Pisa, Largo Lucio Lazzarino, 1- 56121 Pisa (PI), Italy;* [b] *Institute of Information Science and Technologies 'A. Faedo', National Research Council of Italy, Via G. Moruzzi 1, 56124 Pisa, Italy*

*corresponding author linda.giresini@unipi.it

Experimental and numerical investigation on a passive control system for the mitigation of vibrations on SDOF and MDOF structures: mini Tribological ROCKing Seismic Isolation Device

This paper illustrates the results of an experimental campaign performed on a scale prototype of a base dissipator called Mini Tribological ROCKing Seismic Isolation Device. Four superstructures are tested - a shear type frame, braced and unbraced, a multi-storey frame and a SDOF oscillator - with 96 ambient vibration and impulsive tests. An analytical model is illustrated and validated by the experimental tests. The reduction of relative displacement demand is analyzed for all the cases together with the reduction of the acceleration demand, showing remarkable positive effects of the base dissipator on the dynamic behavior of all the superstructures.

Keywords: Damage Avoidance Design, rocking, seismic protection, base isolation, vibration control, friction

1. Introduction

Seismic control systems modify the dynamic characteristics of the superstructure bringing it to a lower frequency and dissipating or transferring earthquake energy through passive, semi-active or active systems. An extensive state-of-art of passive control systems is discussed in [1], whereas an overview about active control system is given in [2]. The main disadvantage of active or semi-active control systems is their need of external power supply, which can be incompatible with high-intensity earthquakes and is not also a sustainable solution. Among the passive seismic protection systems, the viscous-elastic dampers and friction pendulum isolators are much known and widely used. They belong to the category of energy dissipators (friction dampers and fluid viscous dampers) and base isolators (friction pendulum systems and laminated rubber bearings), different from tuned dampers, still passive control devices [1]. The viscous-elastic dampers have the great advantage of being able to simultaneously reduce both accelerations and displacements [3]. Double and triple friction pendulum isolators imply sliding of the superstructure on two or more curved surfaces that re-center it thanks to friction and inertia forces [4–6]. All of them were used both at the base of the structure and at special pivots (center or extremities of bracing systems, beam-to-column joints).

In case of slender structures, such as towers and generic artworks or non-structural objects (steles, statues, busts, showcases, cabinets, etc.), these devices are placed at the base. Some researchers investigated the use of double concave curved surface sliders for marble sculptures [7], statues [8,9] and busts [10]. In case of multiple art objects exhibited in museums, others proposed base isolated floors consisting in double friction pendulum isolators that allow protecting more objects with structural optimization and saving of resources [11]. The analytical approach for passive vibration control of art objects is presented in [12], where the equations of motion of art objects assumed as rigid bodies are derived with the transition from rest, sliding and rocking are considered. All these devices work through a smooth rocking behavior, different from the non-smooth rocking behavior that can be also used as dynamic control system [13–19]. Critical aspects on the resonance conditions of systems assumed as rigid bodies [20,21] and stochastic approaches [22,23] should also be considered.

A special class of passive control system couples the phenomenon of energy dissipation with the modification of the structural dynamic properties. In particular, recently a seismic isolator, called Tribological ROCKing Seismic ISolation Device (TROCKSISD) has been conceived by M. Froli. TROCKSISD is an articulated device that protects the superstructure from shocks and vibrations induced by dynamic actions. The conceptual idea of this device, whose design follows the performance based seismic design criteria, is extensively illustrated in [24]. This isolator is suitable to protect from earthquakes or base vibrations slender structures such as towers or art objects with small dimensions.

The device is composed by two main components in contact through spherical surfaces and a set of elastic dampers (Figure 1). Two are the sources of energy dissipation: the frictional surfaces, whose effect can be tuned with the precompression of peripheral springs, and the viscous dampers mounted in parallel with springs (Figure 1a). The springs co-axial to the dampers dissipate energy and re-center the superstructure.

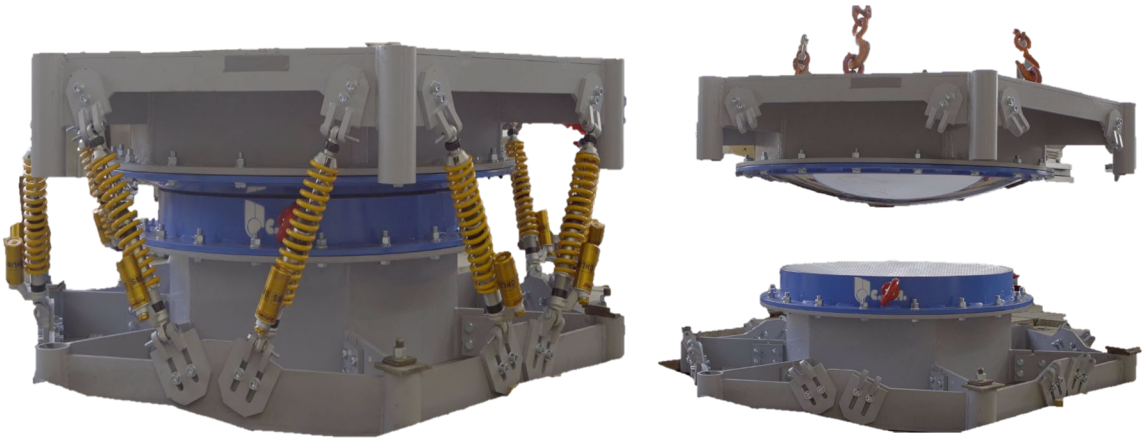

(a) (b)

Figure 1 TROCKSISD prototype (a) with the view of spherical frictional surfaces (b).

This paper illustrates the results of an experimental campaign performed on a scale prototype of TROCKSISD, called miniTROCKSISD (MT). This campaign has the aim of validating the theoretical approach proposed in [24,25] for this class of passive control systems. Section 2 illustrates the experimental tests performed on four superstructures mounted on MT. Section 3 discusses the experimental outcomes comparing the dynamic behavior of the non-isolated structure with the structure isolated through MT. In Section 4 an analytical model of the tested configurations is proposed and numerical tests are carried out to validate it by cross-checking the experimental results in Section 5.

2. Mini Tribological ROCKing Seismic ISolation Device – Mini TROCKSISD

2.1 Description of the specimens

The device shown in Figure 1, whose planar dimension is about 2x2 m^2, is studied in this paper through ascale and 2-dim device (Figure 2). The spherical configuration of the interface (Figure 1b) is modified into a circular shape to simplify the smooth rocking, switching it from 3D motion to an in-plane motion.

The main components of MT (Figure 2) and their functions are summarized in the following.

- The superstructure (Figure 3a) represents the object to protect from vibrations induced by earthquakes or in general by dynamic actions. It is composed by multi-hole bars to connect with masses for realizing multiple configurations.

- The convex cylindrical plate, centered in O (Figure 3b), is the main component where smooth rocking occurs. Through its surface, energy is dissipated by friction on a ETFE sheet, which, in turn, is connected to the concave plate underneath it.
- The concave cylindrical plate (Figure 4) is made of a curved steel plate installed on a ribbed support. The basement is a 20 mm thick base plate of dimensions 370 mm x 278 mm and has 6 threaded holes to allow the placement of bracket connections, which accommodate the bottom part of the viscous elastic devices. The basement has four wheels. Two lateral restraints prevent possible out of plane mechanisms that can occur during the test.
- Pairs of viscous-elastic dampers connect the upper plate of the convex sector and the plate of the basement. These devices are used to add stiffness (k), damping (c), and re-centering capacity to the system.

The specimen has a total height of 727 mm, including the superstructure that spans for485 mm. The total width and depth of the device are respectively 370 mm and 278 mm. As for the materials, common steel is used for all the components, while the sliding surfaces are made of stainless steel and anodized aluminum.

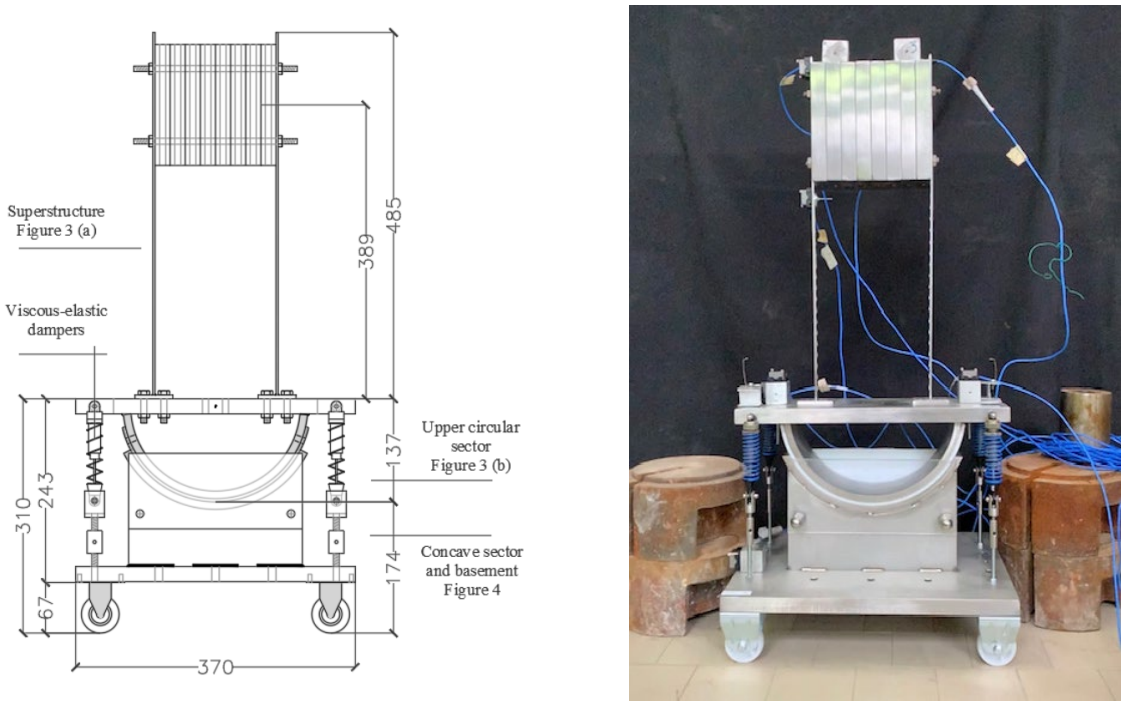

(a) (b)

Figure 2 Overall view of MT with indication of the main components(units in mm) (a) and the device assembled in the laboratory (b).

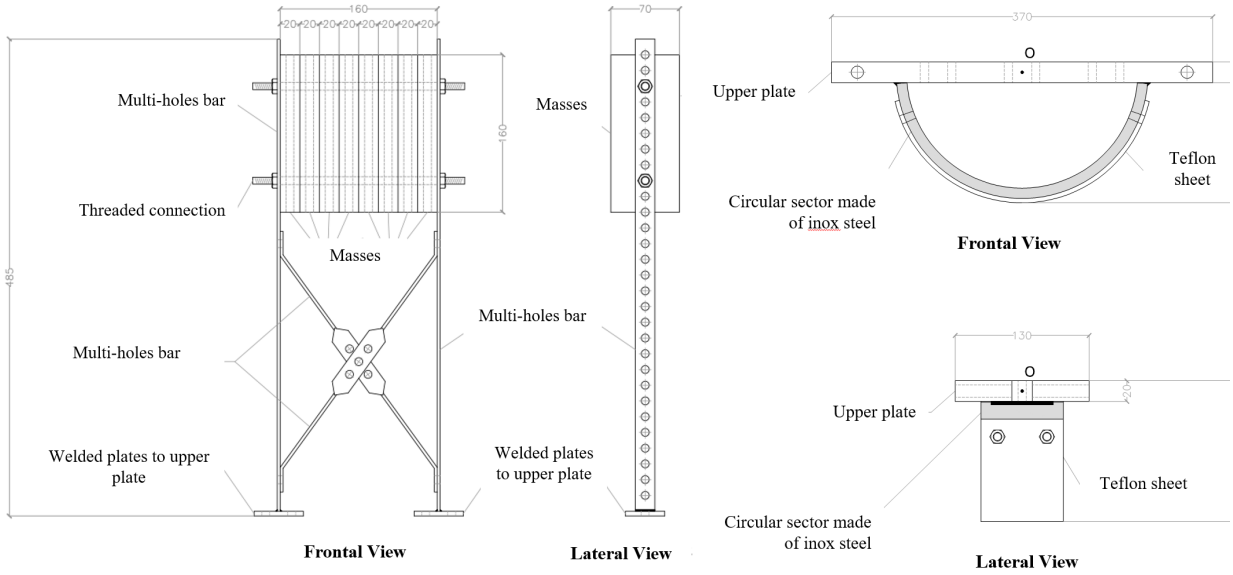

(a) (b)

Figure 3 Superstructure (a) and upper circular sector of MT (b) (units in mm)

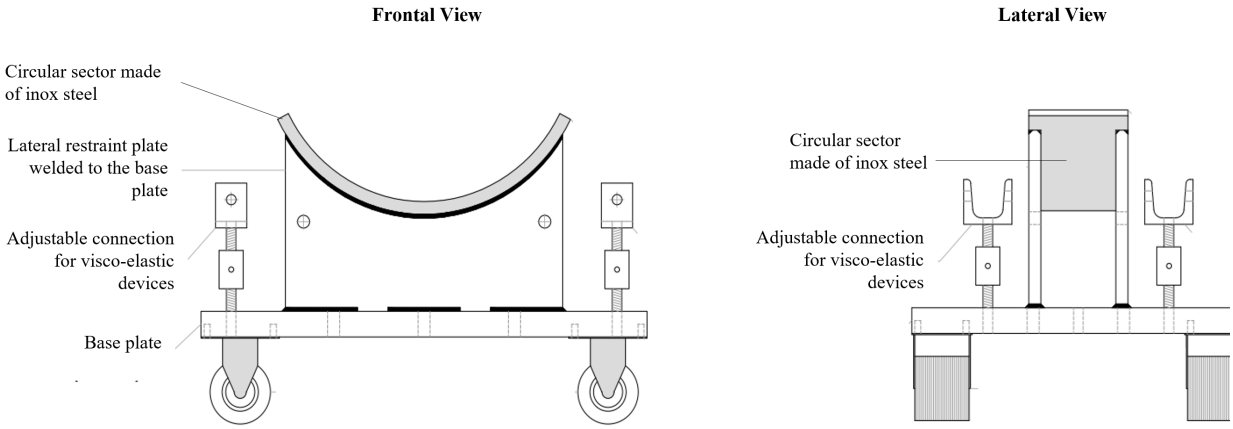

Figure 4 Concave sector and basement of MT (units in mm)

2.2 Experimental test setup of MT

The MT is tested to understand its capabilities in isolating a generic superstructure from vibrations and in dissipating energy provided by earthquake-type actions. From a mechanical point of view, the MT dynamic response strongly depends on the mass and stiffness of the superstructure, on the stiffness and damping of the lateral dissipative devices and on the friction developed at the interface of the two cylindrical plates (§ 2.1).

Typical configurations of the superstructure, frequently found in real cases, are taken into account. They vary in terms of mass and bars disposal and can be associated to Single Degree Of Freedom (SDOF) or Multiple Degrees Of Freedom (MDOF) models, as specified below. Each scheme is preliminary tested in a non-isolated setting in order to evaluate the effect of the isolation provided by the MT on the dynamic response of the system.. In particular, four schemes are considered (Figure 5); each one is labeled with an acronym composed by the number of vertical elements (2P or 1P, where P stands for "pillars"), the number of masses (4M or 8M) and the system to counteracts horizontal actions (bracing system, X, shear-type, T and cantilever, V). Each mass is of 1.75 kg. The first and the second schematics count eight masses; the first one is braced. The third and the fourth schematics have a total of four masses; the third one is a shear-type frame and the last one a cantilever with a single vertical element, similar to the traditional SDOF oscillator.

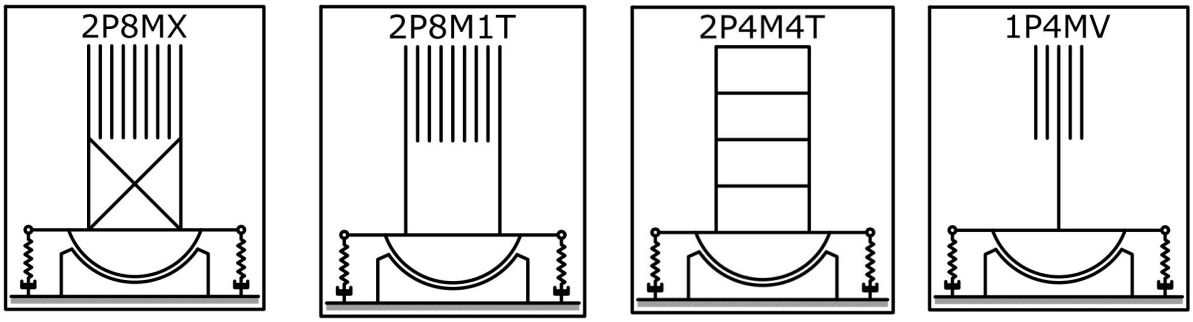

Configuration 1: shear-type frame with bracing

Configuration 2: shear-type frame

Configuration 3: multi-storey shear type frame

Configuration 4: concentrated mass at the top (tank type)

Figure 5 The four configurations tested in the experimental tests

Each schematic corresponds to simplified SDOF and MDOF systems. In particular, schemes C_1, C_2 and C_4 are 2DOF systems: the degrees of freedom are the translation of the superstructure in the horizontal direction and the rotation $\boldsymbol{\alpha}$ of the base around the pivoting point (Figure 6). Scheme C_3 is a 5DOF system: four horizontal translations of each storey and the rotation $\boldsymbol{\alpha}$ of the base around the pivoting point.

As already pointed out, two conditions are investigated: one with the isolation device (defined in the following "with MT") and another one in which the superstructure is not isolated and fixed at the base ("without MT"). Moreover, two dynamic tests are performed to dynamically identify the structure: an ambient vibration test and an impulsive test, where the force has been provided

by a calibrated impact hammer. Two ambient vibration tests are performed for each schematic and for each condition for a sampling time of 7 minutes., for a total number of 16 tests. In addition, 10 impulsive tests, with an instrumented hammer, have been carried out for each schematic and for each condition, for a total number of 80 tests. The instrument used here is an impact hammer PCB Piezotronics Model 086D20, equipped with a transducer tip of average hardness 084A62. The outputs of the 96 tests are measured in terms of accelerations given by accelerometers, disposed as shown in Figure 7.

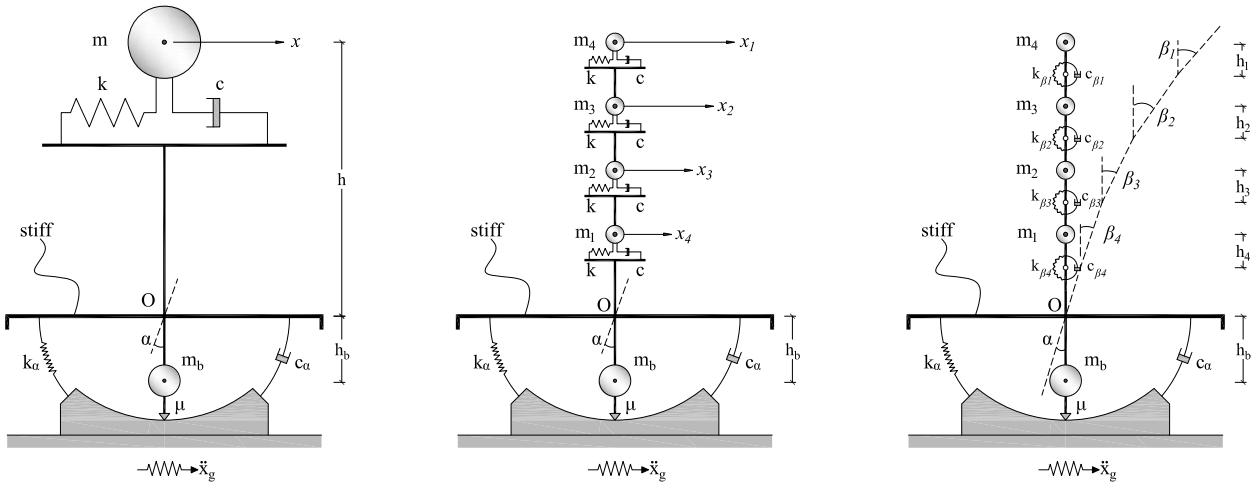

(a) (b) (c)

Figure 6 Single Degree of Freedom (a) and Multiple Degrees of Freedom (b,c) systems representative of the four configurations tested

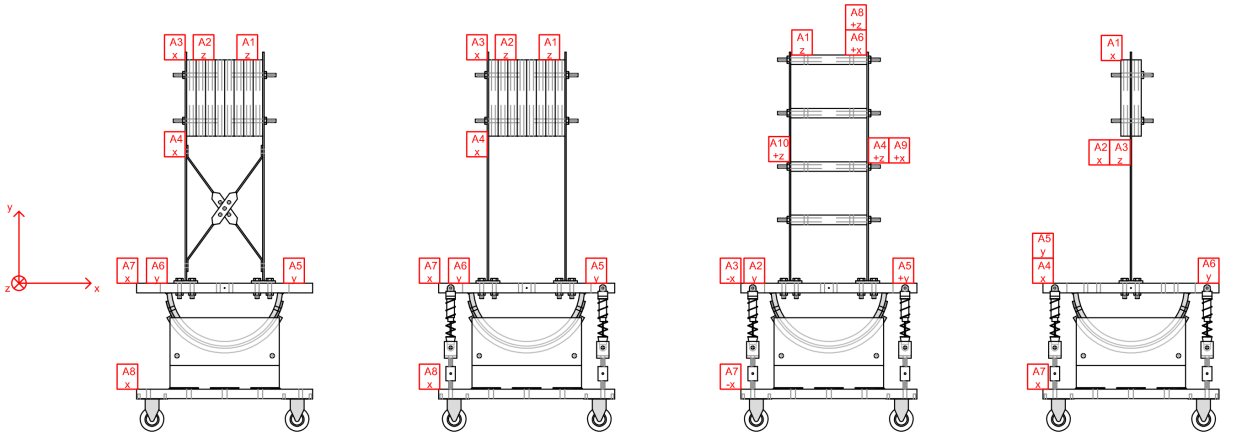

Configuration 1: shear-type frame with bracing

Configuration 2: shear-type frame

Configuration 3: multi-storey shear type frame

Configuration 4: concentrated mass at the top (SDOF oscillator)

Figure 7 Disposition of accelerometers in the tested configurations

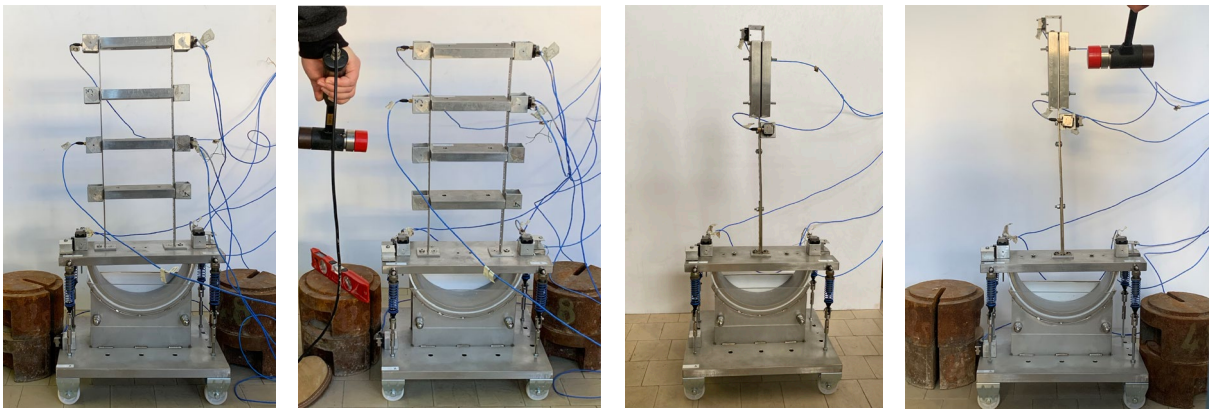

(a) (b) (c) (d)

Figure 8 Configuration C_3 (a, b) and C_4 (c, d) tested with impulsive force applied through a calibrated hammer

2.3 Experimental test setup on single components

Before testing the assembled prototype, several tests on individual components are performed to identify their mechanical characteristics. This step is necessary to acquire reliable mechanical parameters for the phase of cross validation of the analytical model presented in Section 4. The individual components constitute the viscous-elastic dampers and the interface between concave and convex sectors - described in § 2.1. More in detail, three single tests are carried out: one on the springs, able to re-center the superstructure during the smooth rocking, another one on the dampers, which dissipate energy over motion, and the last one on the concave surface to measure the frictional moment.

2.3.1 Tests on springs

The springs are part of the viscous-elastic dampers and are tested separately from the damper. Each spring is located between two rigid plates; the upper plate is loaded with additional masses (each one of about 300 grams) that cause the spring compression. The axial load is applied through five subsequent steps by increasing the masses on the upper plate. Each measurement is performed twice by means of linear variable displacement transducers (LVDT) and mean values are considered. The outputs are acquired with a time interval of 2 seconds. Each data set approximately contains 100 values of displacement. The stiffness of the springs is computed by calculating the inclination of the force-displacement relationship as discussed in § 3.1.

2.3.2 Tests on dampers

The tests on the dampers are performed similarly to the tests on the springs. The damper is compressed between two rigid plates by the masses, which are gradually added to an upper rigid plate. In particular, four subsequent loads are applied: 0.93, 1.25, 1.57, 2.22 daN. Once that the compression of the damper reaches a stable value, the load is removed and the return velocity is measured to get the equivalent viscous coefficient. For each of the fours dampers, each test is repeated twice.

2.3.3 Tests on the frictional cylindrical surface

A fundamental mechanical parameter that influences the smooth rocking is the friction at the interface between convex sector and concave sector. For this reason, a static test is performed to assess the static friction coefficient. In particular, a load manually applied by pouring sand into a bucket causes the device to rotate. The force necessary to trigger the mechanism is registered and by means of the Coulomb's model the frictional coefficient is calculated. To assess the amount of friction, a static test is performed twice for each direction of rotation.

3. Results and discussion of the experimental tests

This section contains a summary of the most important experimental results and discusses them in terms of dynamic response and effectiveness of the MT device, compared with the condition without base isolation.

3.1 Mechanical features of the single components

The tests on **springs** described in § 2.3.1 allow obtaining the force-displacement relationships displayed in Figure 9. From them, it is immediate to calculate values of spring stiffness k ranging from 0.55 to 0.70 daN/cm. The average value of stiffness is equal to 0.67 daN/cm.

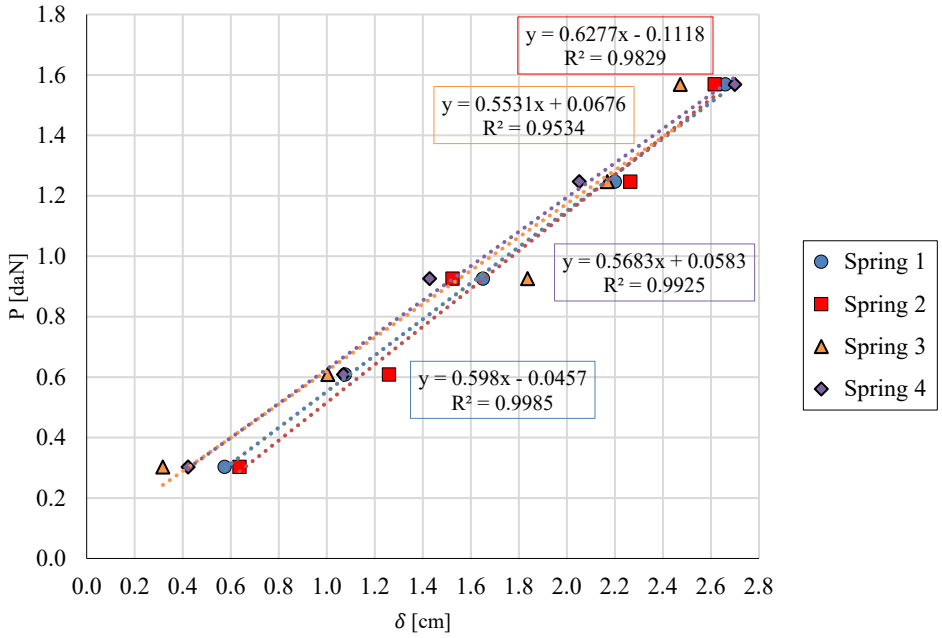

Figure 9 Force-displacement relationships of the springs used in MT

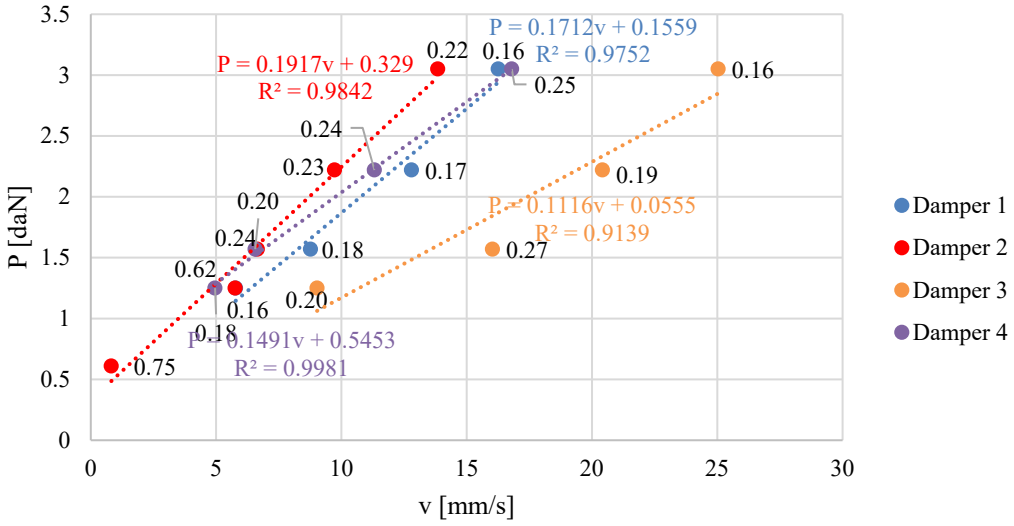

Figure 10 Force-velocity relationships of the assembled dampers used in MT

As for the tests on the **dampers**, the viscous constant is calculated by adopting the Kelvin's solid model. In particular, given $s(t_1)$ the maximum displacement measured by the LVDTs at time t_1, F_0 the applied force, one can obtain the viscous constant η from the following expression:

$$s(t_1) = \frac{F_0}{k}\left(1 - e^{-\frac{t_1 k}{\eta}}\right) \tag{1}$$

Figure 10 displays the force-velocity relationships of the four assembled dampers tested with the interpolating curves. The results show that the viscous constant changes depending on the applied load and it passes from 1.56 daNs/cm to 3.03 daNs/cm.

For what concerns the tests on the **frictional surface**, as stated in § 2.3.3, a horizontal load is manually applied by pouring sand into a bucket. This causes the rotation of the device in counter-clockwise direction (Figure 11a). The moment of the applied load $F \cdot b$ is balanced by the frictional moment M_μ as follows:

$$F \cdot b = M_\mu = \mu_s N \cdot R \tag{2}$$

Where b is the lever arm of the force F and R is the radius of the cylindrical surface (Figure 11a). The test is performed by applying the force F in both horizontal directions $\mp x$. From Equation (2), it is immediate to obtain the value of the static friction coefficient μ_s. The results show that, test after test, the coefficient slightly changes and its average value, obtained neglecting the maximum and minimum values, is about 0.22 (Figure 11b).

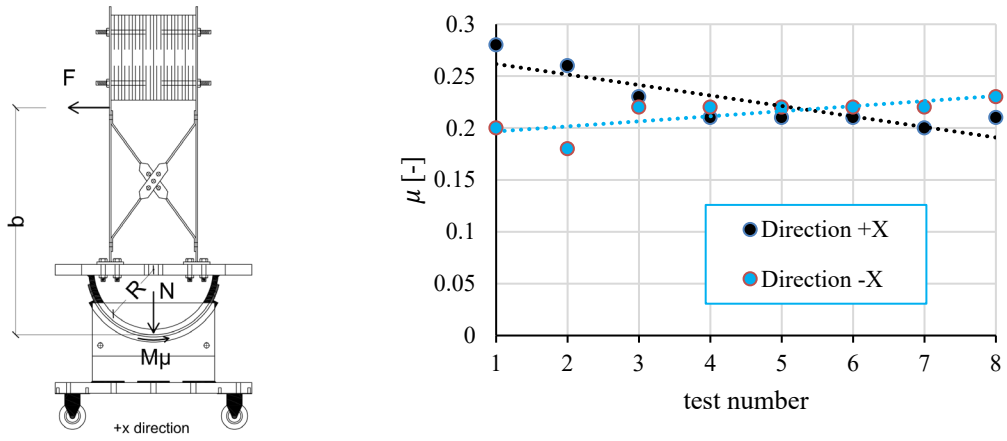

(a) (b)

Figure 11 Determination of static friction coefficient at the cylindrical interface: experimental set-up (a) and results (b).

3.2 Comparison between isolated and non-isolated superstructure

This paragraph discusses the comparison between the superstructure isolated by MT and superstructure fixed at its base. The ambient vibrations tests give the dominant frequencies of the

four configurations in x direction (in-plane) and in z direction (out-of-plane). The results highlight that the isolated superstructure is characterized by eigenfrequencies lower than those of the non-isolated superstructure, as expected (first row of Table 1). This beneficial effect, which is visible in particular for configuration C_4 , in which a reduction by 15% is obtained. Other than for C_4, the maximum reduction of eigenfrequency is obtained for C_3, with a difference by about 11%.

It is worthy to observe that this effect is associated to a reduction of spectral acceleration for the isolated structure. To investigate this beneficial aspect, one can examine the acceleration time-histories for both scenarios of the four configurations. The comparison of the results obtained by applying an impulsive force through a calibrated hammer are reported in Figure 12. These acceleration time histories are selected from the 80 tests considering similar amplitudes of impulsive inputs. As an example, the first configuration has an acceleration peak of 9 m/s^2 that reduces to 7.6 m/s^2 in case of isolation (Figure 12a). The strongest reduction is mostly visible for the shear type frames, both unbraced and braced, at a larger extent for the unbraced configuration (Figure 12a-b).

Table 1 Dominant experimental eigenfrequencies obtained from ambient vibration tests on the superstructure with MT and on the non-isolated superstructure (without MT)

	C1 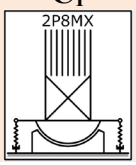			**C2** 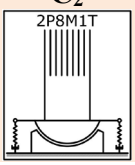			**C3** 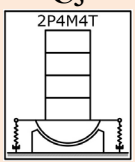			**C4** 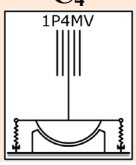		
	MT ×	**MT ✓**	**Δw/o-With (%)**	**MT ×**	**MT ✓**	**Δw/o-With (%)**	**MT ×**	**MT ✓**	**Δw/o-With (%)**	**MT ×**	**MT ✓**	**Δw/o-With (%)**
f_{exp} [Hz]	16.8	15.6	-6.9%	2.4	2.3	-7.4%	9.6	8.6	-10.6%	2.6	2.2	-15.1%
f_{num} [Hz]	16.5	16.2	-1.5%	2.6	2.4	-8.0%	10.3	8.6	-16.1%	2.6	2.4	-9.5%
$\Delta_{exp-num}$ (%)	-1.8%	3.8%		7.8%	7.1%		7.3%	0.7%		1.5%	8.2%	

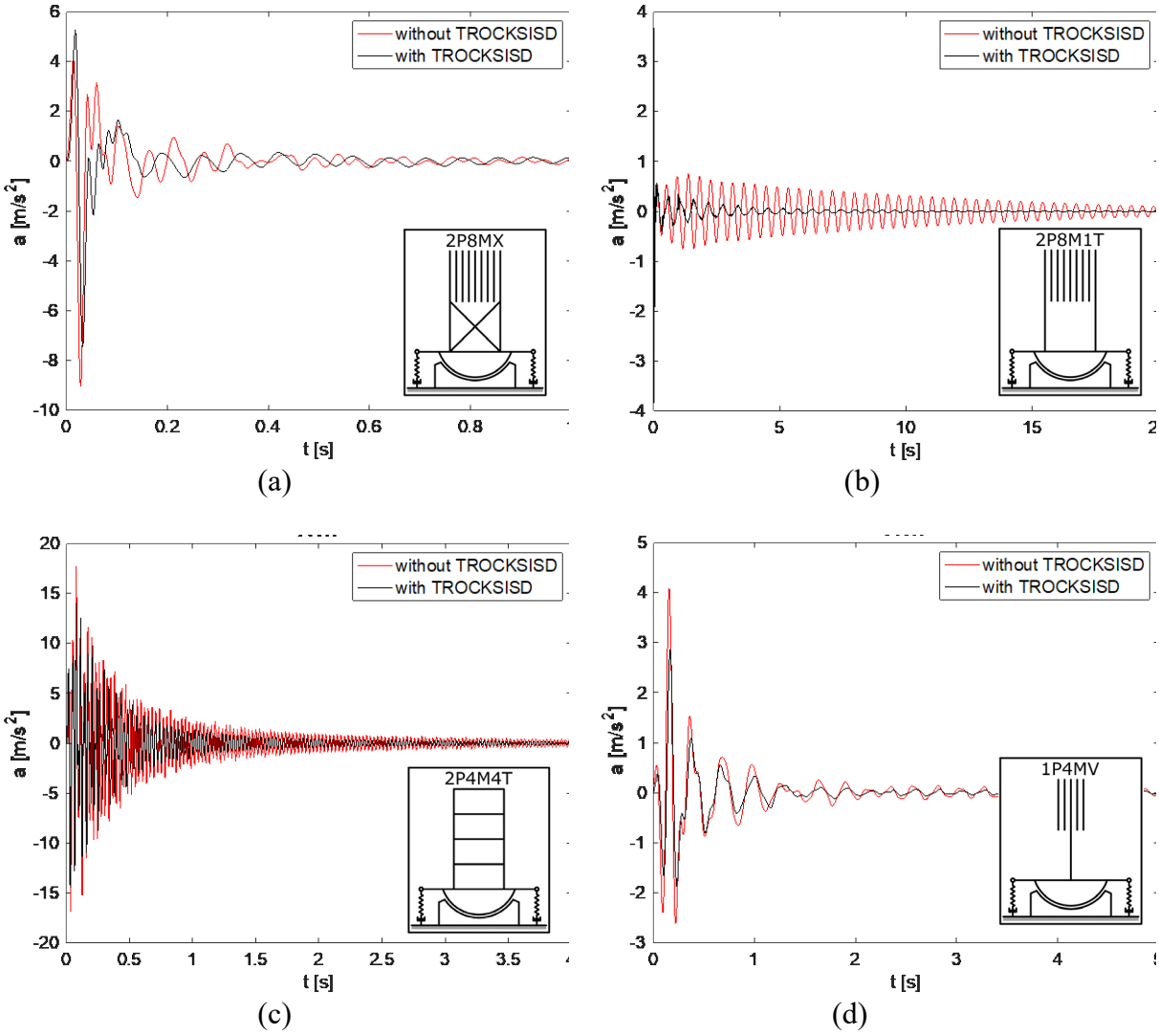

Figure 12 Comparisons between acceleration time histories of isolated and non-isolated superstructure: C_1 (a), C_2 (b), C_3 (c), C_4 (d)

Considering the maximum peaks after the application of the impulsive force, the reduction from the non-isolated to the isolated structure is by 17%, 13%, 14% and 30% respectively for configuration C_1, C_2, C_3 and C_4. The velocity and displacement time histories are obtained by integration of the acceleration time history of each configuration. The contemporary reduction of acceleration response and increase of displacement demand are shown for the braced frame in Figure 13: the reduction of maximum displacement is by 56%. Instead, for the cantilever SDOF oscillator (C_4), the same reduction is by 46%, but the displacement values are one order of magnitude higher than those of C_2 (Figure 14). Therefore, even if the reduction of eigenfrequency of C_4 is only half of C_2 (Table 1), the reduction of maximum displacement is still remarkable.

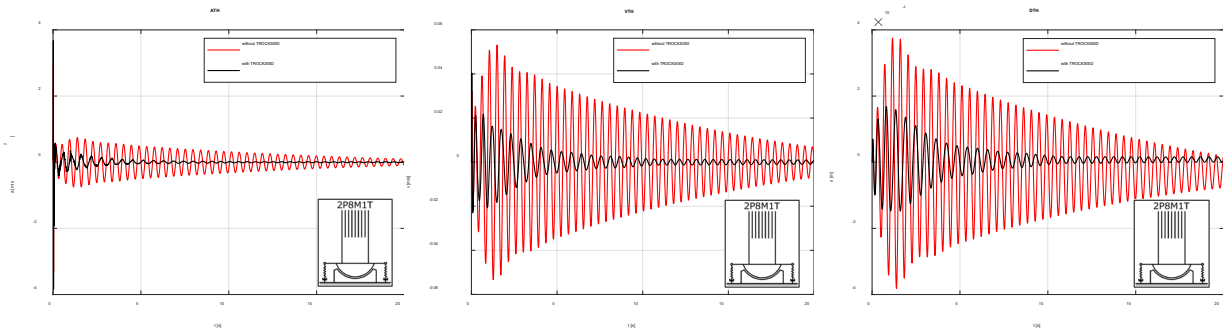

(a) (b) (c)

Figure 13 Braced frame structure (C_2): acceleration (a), velocity (b), displacement (c) time histories

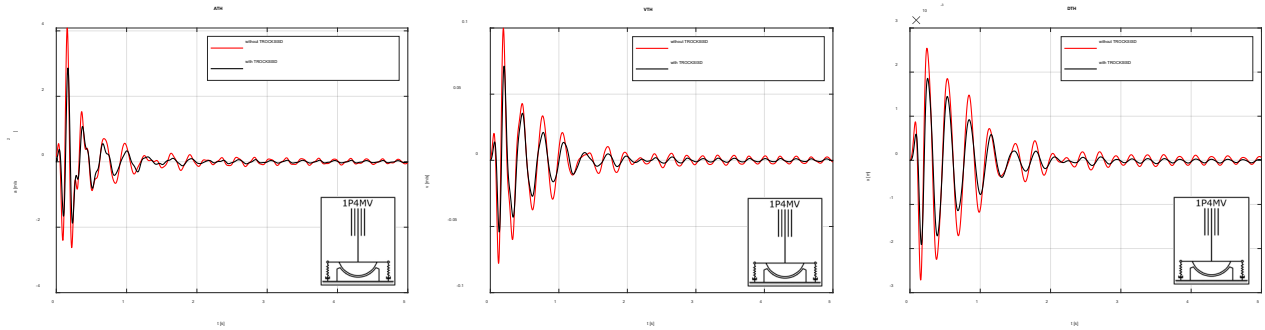

(a) (b) (c)

Figure 14 SDOF oscillator (C_4): acceleration (a), velocity (b), displacement (c) time histories

4. Analytical model and numerical analyses

4.1 Equations of motion

The analytical model here introduced simulates the dynamic behavior of the four superstructures with and without MT. The results predicted by the analytical model are cross-checked with the experimental results. Two different analytical models can be considered, one for the non-isolated superstructure and another for the superstructure isolated by MT.

As for the non-isolated superstructure of mass m and stiffness k, the cases of SDOF systems (configurations 1, 2 and 4 of Figure 5) are trivially solved by calculating the cyclic frequency with the well-known expression $f = 2\pi\sqrt{m/k}$. The eigenfrequencies of C_3 can be easily obtained by solving the equations of motion in free vibration regime for MDOF systems.

When the isolated superstructure is considered, an additional degree of freedom, that is the rigid rotation $\boldsymbol{\alpha}$ of the base isolator, has to be taken into account. For the 2DOF system (rotation $\boldsymbol{\alpha}$ and horizontal displacement $\boldsymbol{x}$, Figure 6a), the equations of motion are [24]:

$$\begin{cases} \mathrm{m}\ddot{x} + \mathrm{c}\dot{x} - \mathrm{ch}\dot{\alpha} + \mathrm{k}x - \mathrm{kh}\alpha = -\mathrm{m}\ddot{x}_g \\ I_\mathrm{b}\ddot{\alpha} + \left(\mathrm{c}_\varphi + ch^2\right)\dot{\alpha} + \left(\mathrm{k}_\varphi + \mathrm{k}h^2\right)\alpha - \mathrm{ch}\dot{x} - khx + \mathrm{M}_\mu = -m_b h_b \ddot{x}_g \end{cases} \tag{3}$$

Where c is the equivalent viscous coefficient of the superstructure, h the distance between center of rotation O and center of mass of the superstructure, $\ddot{x}_g$ the seismic acceleration time history. Moreover, I_b is the inertia moment of MT, c_α and k_α respectively the rotational viscous coefficient and stiffness, h_b the distance between the center of rotation O and the center of mass of MT. M_μ stands for the frictional moment developed at the interlayer between the two cylindrical surfaces.

The modal analysis is performed by solving the eigenvalues problem associated to the following system:

$$\begin{cases} \mathrm{m}\ddot{x} + \mathrm{c}\dot{x} - \mathrm{ch}\dot{\alpha} + \mathrm{k}x - \mathrm{kh}\alpha = 0 \\ I_\mathrm{b}\ddot{\alpha} + (\mathrm{c}_\alpha + ch^2)\dot{\alpha} + (\mathrm{k}_\alpha + \mathrm{k}h^2)\alpha - \mathrm{ch}\dot{x} - khx = 0 \end{cases} \tag{4}$$

obtained by neglecting the external excitation term and the frictional moment.

As for configuration C_3, one needs to write the equations of motion of a five degrees of freedom system (shown in Figure 6b) in terms of translational degrees of freedom:

$$\begin{cases} m_1\ddot{x}_1 + k_1 \cdot (x_1 - x_2) = -\mathrm{m}_1\ddot{x}_g \\ m_2\ddot{x}_2 + k_2 \cdot (x_2 - x_3) - k_1 \cdot (x_1 - x_2) = -\mathrm{m}_2\ddot{x}_g \\ m_3\ddot{x}_3 + k_3 \cdot (x_3 - x_4) - k_2 \cdot (x_2 - x_3) = -\mathrm{m}_3\ddot{x}_g \\ m_4\ddot{x}_4 + k_4 \cdot (x_4 - h_4 \cdot x_5) - k_3 \cdot (x_3 - x_4) = -\mathrm{m}_4\ddot{x}_g \\ I_\mathrm{b}\ddot{\alpha} + c_\alpha\dot{\alpha} + k_\alpha\alpha - k_4 \cdot (x_4 - h_4 \cdot \alpha) + \mathrm{M}_\mu = -m_b h_b \ddot{x}_g \end{cases} \tag{5}$$

or, in terms of rotational degrees of freedom:

$$\begin{cases} \mathrm{I}_{m1}\ddot{\beta}_1 + c_{\beta1}\left(\dot{\beta}_1 - \dot{\beta}_2\right) + k_{\beta1}(\beta_1 - \beta_2) = -\mathrm{m}_1\ddot{x}_g h_1 \\ \mathrm{I}_{m2}\ddot{\beta}_2 + c_{\beta2}\left(\dot{\beta}_2 - \dot{\beta}_3\right) - c_{\beta1}\left(\dot{\beta}_1 - \dot{\beta}_2\right) + k_{\beta2}(\beta_2 - \beta_3) - k_{\beta1}(\beta_1 - \beta_2) = -\mathrm{m}_2\ddot{x}_g h_2 \\ \mathrm{I}_{m3}\ddot{\beta}_3 + c_{\beta3}\left(\dot{\beta}_3 - \dot{\beta}_4\right) - c_{\beta2}\left(\dot{\beta}_3 - \dot{\beta}_3\right) + k_{\beta3}(\beta_3 - \beta_4) - k_{\beta2}(\beta_2 - \beta_3) = -\mathrm{m}_3\ddot{x}_g h_3 \\ \mathrm{I}_{m4}\ddot{\beta}_4 + c_{\beta4}\left(\dot{\beta}_4 - \dot{\alpha}\right) - c_{\beta3}\left(\dot{\beta}_3 - \dot{\beta}_4\right) + k_{\beta4}(\beta_4 - \alpha) - k_{\beta3}(\beta_3 - \beta_4) = -\mathrm{m}_3\ddot{x}_g h_4 \\ I_\mathrm{b}\ddot{\alpha} + c_\alpha\dot{\alpha} - c_{\beta4}\left(\dot{\beta}_4 - \dot{\alpha}\right) - k_{\beta4}(\beta_4 - \alpha) + \mathrm{M}_\mu = -m_b h_b \ddot{x}_g \end{cases} \tag{6}$$

where $\mathbf{I}_{mi}$ is the inertia moment of the i-th mass, $\boldsymbol{c_{\beta i}}$ and $\boldsymbol{k_{\beta i}}$ respectively the rotational damping coefficient and the rotational stiffness associated to the i-th mass. The five lagrangian parameters

are the rotation $\boldsymbol{\beta_i}$ of the i-th mass and the base rotation $\boldsymbol{\alpha}$. Finally, the distances from the masses $\boldsymbol{h_i}$ are reported in Figure 6c.

These distances are constant and equal to h for the case under examination. Moreover, to validate the experimental results with forced vibration tests with calibrated hammer, $\ddot{x}_g = 0$ and only the third degree of freedom (Figure 8b) has been forced. For it, $-\mathrm{m}_3\ddot{x}_g = F$ where F is the impulsive force exerted by the hammer.

Again, to obtain the modal properties the eigenvalues problem with null friction moment and external excitation is solved.

Table 2 Mechanical parameters adopted in the analytical model to perform numerical analyses

Parameter	C_1	C_2	C_3	C_4
$\mathbf{m_s}$ **[kg]**	14.2	14.2	7	3.7
$\mathbf{k_s}$ **[N/m]**	150000	3823	80400	600
$\mathbf{k_\alpha}$ **[Nm]**	30.7	30.7	30.7	30.7
$\mathbf{c_\alpha}$ **[Nms]**	57	57	100	57
Mμ [Nm]	7.5	7.5	2	4.5

The complete equations of motion are numerically solved via a MATLAB code [26] specifically written considering both free vibration and impulsive forces with the aim of comparing numerical results with experimental tests.

4.2 Validation of the analytical model

The responses predicted by the numerically solved analytical model are here compared to experimental results to verify its reliability. The third row of Table 1 Δ (%) lists the percentage differences between the eigenfrequencies obtained with the numerical model and those given by the corresponding experimental tests. The considered scenario is that of the isolated structure, that is when the structure is equipped with MT. The results in terms of eigenfrequencies are in excellent agreement for configurations C_1 and C_3 (differences by less than 5%) and in very good agreement for C_2 and C_4, with maximum difference by about 8% (Table 1).

As for the comparison between displacement time-histories (TH), Figure 15 displays experimental and numerical outputs of the four configurations. The numerical TH are calculated through integration of the acceleration TH provided by the accelerometer. The calculation is performed according to the method illustrated in [27]. The experimental outputs have been filtered in the range of frequency 2-50 Hz and compared with the TH predicted by the analytical model solving Eqs. (3) and (5).

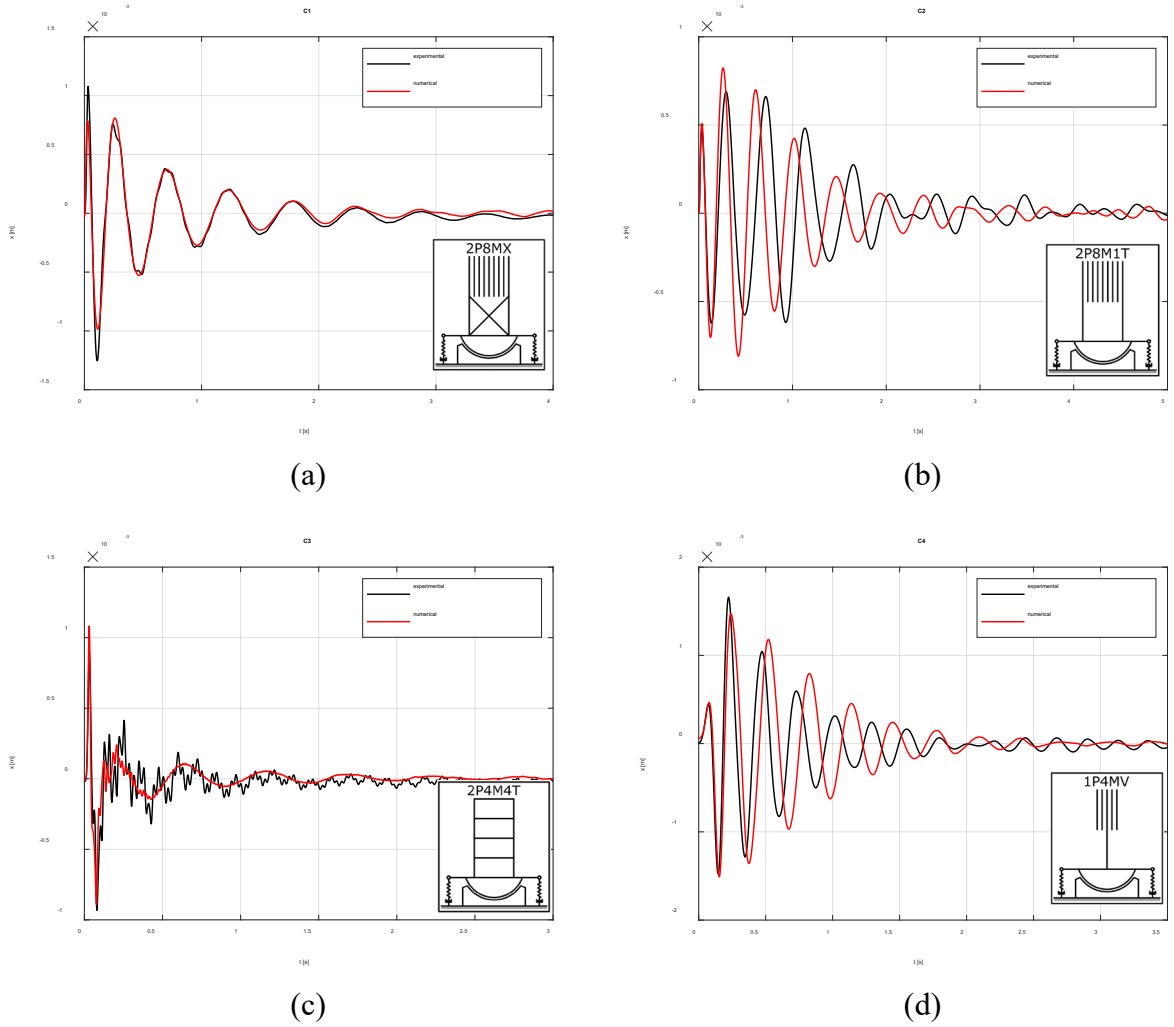

(a) (b)

(c) (d)

Figure 15 Comparisons between experimental and numerical displacement time-histories for the four configurations: C_1 (a), C_2 (b), C_3 (c), C_4 (d)

One can observe that the results are in good agreement for C_1 (shear-type frame with bracing): even though the first peak is underestimated by the numerical analysis, the following peaks are perfectly the same (Figure 15a). In this case the lowest value of viscous-elastic damping obtained from experimental tests on the single components has been assumed (§ 3.1). Instead, for C_2 (shear-type frame without bracing) the experimental trend is correctly reproduced for the first peaks (Figure 15b). For configuration C_3 the peaks are correctly reproduced even though there are some high frequencies in the experimental output. For configuration C_4 the numerical curve underestimates the response only for the second positive peak, and for the following cycles there is a delay of the numerical response.

4.3 Effectiveness of miniTROCKSISD on different superstructures

This section discusses the beneficial effects provided by the base dissipator in terms of reduction of acceleration demands. Firstly, the dynamic properties of the non-isolated and isolated

superstructure are considered. The frequency of the isolated superstructure f_{MT}, normalized to that of the non-isolated structure f_s, gives the dimensionless frequency plotted in Figure 16 against the normalized stiffness $k_s/k_{s,MT}$, where k_s is the stiffness of each superstructure (in F/L) and $k_{s,MT}$ is the stiffness of the springs belonging to MT. Given that $k_{s,MT} = 600\ N/m$, for all the configurations, although the normalized stiffness spans between 1 and 250, the reduction of eigenfrequency is quite similar, since f_{MT}/f_S spans from 0.85 to 0.93. However, C_1, C_2 and C_3 have a closer behavior, as expected since the fourth configuration is remarkably different from the others. More in detail, C_1 and C_2 only differ from the presence of bracing, which, nevertheless, does not change the modification of the behavior with the base isolator ($\frac{f_{MT}}{f_S} = 0.93$ for both). The similarity of such a reduction is a favorable outcome, since for very different superstructures the change of vibration frequency is unremarkable.

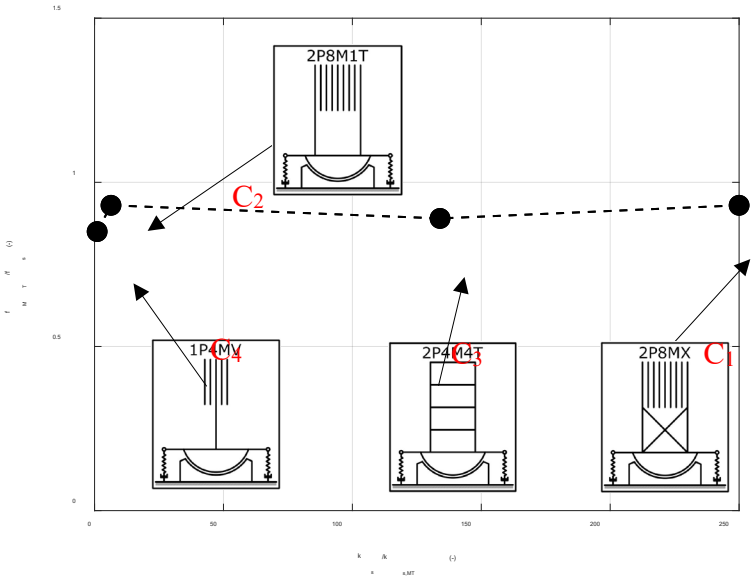

Figure 16 Normalized frequency versus normalized stiffness of the isolated structures

Secondly, the reduction of acceleration demand is calculated for each configuration as follows. In a variable range of time Δt equal to 1 s, 2 s or 5 s, the mean values of acceleration peaks $\bar{a}_j^i$ are considered for each applied impulsive load j (Figure 17a), where i is the configuration label (from C_1 to C_4). The term $\bar{a}_{j,I}^i$ is the input acceleration of the j^{th} impulse. The mean of all the impulsive loads for each configuration is $\bar{a}^i$ and $\bar{a}_{MT}^i$ respectively for the non-isolated and the isolated structure. These values are normalized to the corresponding mean values of the inputs:

$$R_a = \frac{\bar{a}^i}{\bar{a}_I^i};\ R_{a_{MT}} = \frac{\bar{a}_{MT}^i}{\bar{a}_{I,MT}^i} \tag{7}$$

Finally, the percentage of reduction of normalized acceleration peaks reads:

$$\Delta a = \frac{R_a - R_{a_{MT}}}{R_a} \cdot 100 \tag{8}$$

An example of results for configuration C2 is reported in Figure 18b, where the empty dots represent the single R_{aj} for each impulsive test considering different time ranges.

All the results are reported in Figure 18, where the abscissa in the logarithmic scale for the sake of better readability: if one considers the period of 5 seconds, the results are more scattered, whereas for periods of 1 second and 2 seconds the variation of acceleration is quite similar with the exception of C_1. Anyway, the reduction of acceleration demand is between 10% and 40%. The best improvements are registered for C_2 and C_3, which have average values of normalized stiffness $k_s/k_{s,MT}$ equal to about 7 and 140 respectively.

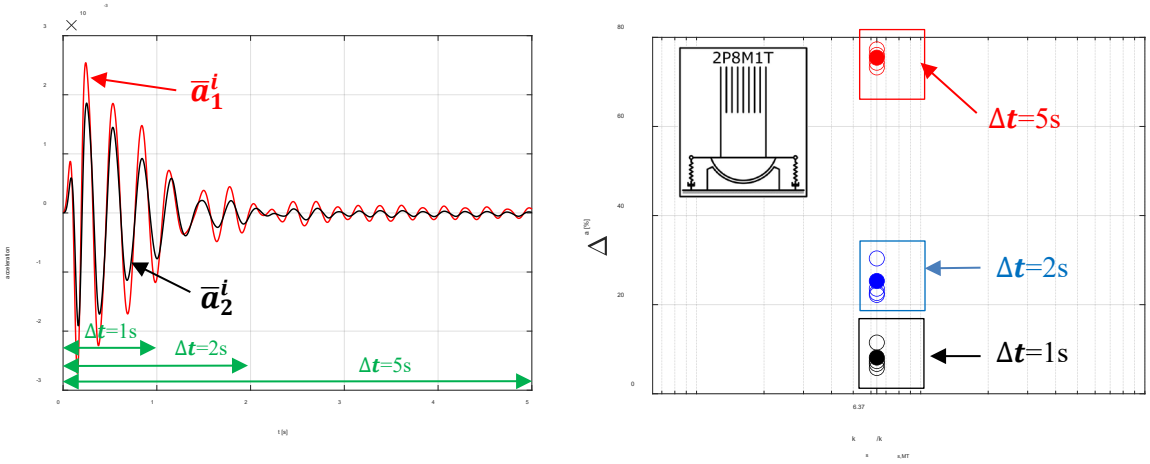

(a) (b)

Figure 17 Methodology for identifying the variation of acceleration from isolated and non-isolated superstructure: selection of two acceleration time histories for configuration C_i and two hammer tests, considering different time ranges (a); average values for each hammer test and for different time ranges for C_2 (b)

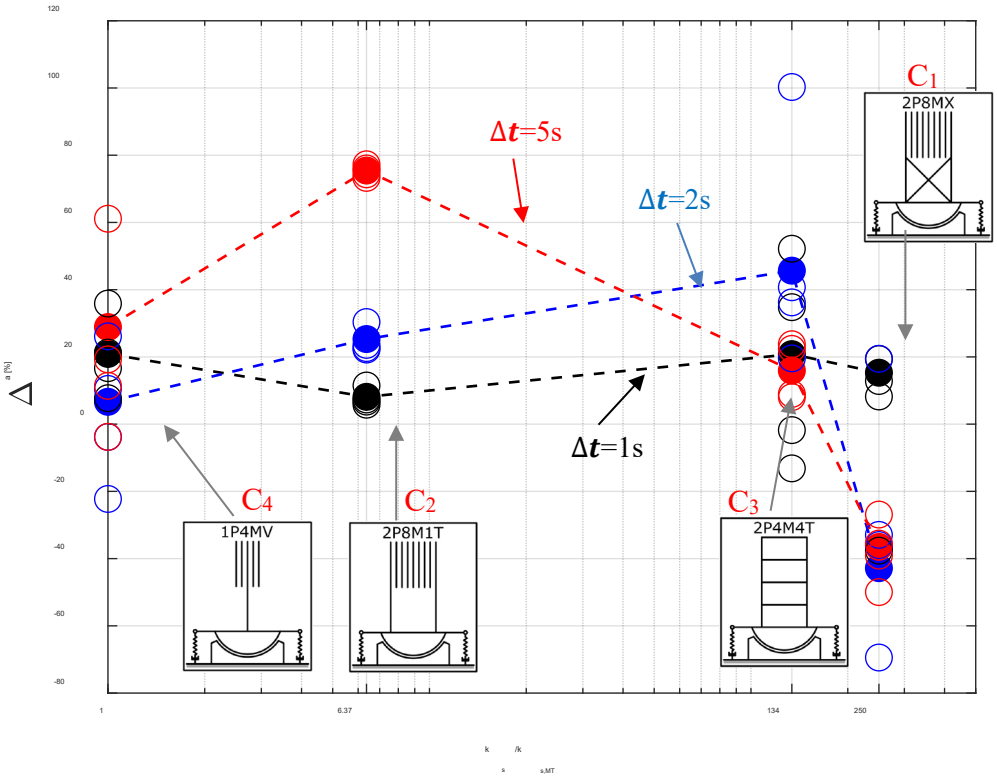

Figure 18 Reduction of acceleration demand in the isolated structures

Conclusions

This paper analyzed the experimental results of 96 dynamic tests on four configurations of steel super-structures isolated with an innovative base dissipator called Mini Tribological ROCKing Seismic Isolation Device (miniTROCKSISD or MT). Tests on single components that constitute the viscous-elastic dampers are performed to identify their stiffness and damping properties, besides a test for measuring the frictional moment developed at the interface between concave and convex cylindrical surfaces. Afterwards, ambient vibrations and impulsive tests were performed on four traditional steel structures that are representative of possible specimen to protect characterized by different mass and flexibility. They allowed calculating the dynamic properties of the isolated structures (tested with and without MT), highlighting reductions of dominant eigenfrequency from 8% to 15%. The larger reduction was obtained for the multi-storey structure, with an experimental reduction of acceleration demand by 30%. Although the reduction of eigenfrequency was not so relevant, the reduction of relative displacement demand was remarkable, between 46% and 56% for the SDOF oscillator and the braced frame structure

respectively. This aspect is of paramount importance, since the stresses on the isolated superstructure are strongly reduced.

Moreover, a specific MATLAB code was written to predict the dynamic performances of such a device by comparing experimental and numerical results. The equations of motion of 2DOF and 5DOF systems were written to model the dynamic response of the isolated superstructures. The numerical results were shown to be in very good agreement with experimental tests both in terms of modal properties and displacements. A method to assess the reduction of acceleration demands from impulsive tests was presented, showing a decrease ranging from 10% to 40% depending on the considered time check range. The superstructures, although very different in terms of normalized stiffness, showed a similar reduction of eigenfrequency and a similar reduction of acceleration demand from 10% to 20%, taking into account as reliable time check range of 1 second. This aspect was shown to be interesting, since, although the normalized stiffness of the superstructures spanned from 1 to 250, a similar improvement was obtained. This issue will be further investigated in the experimental tests on the full scale specimens (Big TROCKSISD).

Acknowledgements

This research has been partially founded by the grants PRA2018-2019 (University of Pisa, grant no. PRA_2018_61) and DT2019 (grant Dimostratori Tecnologici – TROCKSISD 2019, University of Pisa). The authors would like to thank Eng. Emma Vagaggini for the MATLAB calculations and the realization of some figures and Dr. Giuseppe Chellini for the tests setup and the data acquisition.

Data availability statement

The data that support the findings of this study are available from the corresponding author, L.G., upon reasonable request.

References

1. Parulekar YM, Reddy GR. Passive response control systems for seismic response reduction: A state-of-the-art review. *International Journal of Structural Stability and Dynamics* 2009; **09**.
2. Soong TT, Constantinou MC. *Passive and Active Structural Vibration Control in Civil Engineering*. New York: Springer; 1994.
3. Lavan O, Dargush GF. Multi-Objective Evolutionary Seismic Design with Passive Energy Dissipation Systems. *Journal of Earthquake Engineering* 2009; **13**(6): 758–790. DOI: 10.1080/13632460802598545.

4. Fenz DM, Constantinou MC. Behaviour of the double concave Friction Pendulum bearing. *Earthquake Engineering & Structural Dynamics* 2006; **35**(11): 1403–1424. DOI: 10.1002/eqe.589.

5. Castaldo P, Alfano G. Seismic reliability-based design of hardening and softening structures isolated by double concave sliding devices. *Soil Dynamics and Earthquake Engineering* 2020; **129**: 105930. DOI: https://doi.org/10.1016/j.soildyn.2019.105930.

6. Fadi F, Constantinou MC. Evaluation of simplified methods of analysis for structures with triple friction pendulum isolators. *Earthquake Engineering & Structural Dynamics* 2010; **39**(1): 5–22. DOI: 10.1002/eqe.930.

7. Baggio S, Berto L, Favaretto T, Saetta A, Vitaliani R. Seismic isolation technique of marble sculptures at the Accademia Gallery in Florence: numerical calibration and simulation modelling. *Bulletin of Earthquake Engineering* 2015; **13**(9): 2719–2744. DOI: 10.1007/s10518-015-9741-2.

8. De Canio G. Marble devices for the Base isolation of the two Bronzes of Riace: a proposal for the David of Michelangelo. *15th World Conference on Earthquake Engineering*, Lisbon, 24th-28th September 2012: 2012.

9. Borri A, Grazini A. Diagnostic analysis of the lesions and stability of Michelangelo's David. *Journal of Cultural Heritage* 2006; **7**: 273–285.

10. Berto L, Rocca I, Saetta A. Vulnerability assessment methods for rocking and overturning of free standing elements. *Soil Dynamics and Earthquake Engineering* 2018; **110**: 121–136. DOI: https://doi.org/10.1016/j.soildyn.2018.02.010.

11. Sorace S, Terenzi G. Seismic performance assessment and base-isolated floor protection of statues exhibited in museum halls. *Bulletin of Earthquake Engineering* 2015; **13**(6): 1873–1892. DOI: 10.1007/s10518-014-9680-3.

12. Caliò I, Marletta M. Passive control of the seismic rocking response of art objects. *Engineering Structures* 2003; **25**: 1009–1018.

13. Giresini L, Solarino F, Paganelli O, Oliveira D, Froli M. One-sided rocking analysis of corner mechanisms in masonry structures: influence of geometry, energy dissipation and boundary conditions. *Soil Dynamics and Earthquake Engineering* 2019; **Submitted**.

14. Casapulla C, Giresini L, Argiento LU, Maione A. Nonlinear Static and Dynamic Analysis of Rocking Masonry Corners Using Rigid Macro-Block Modeling. *International Journal of Structural Stability and Dynamics* 2019; **19**(11): 1950137. DOI: 10.1142/S0219455419501372.

15. Giresini L, Pantò B, Caddemi S, Caliò I. Out-of-plane seismic response of masonry façades using discrete macro-element and rigid block models. *COMPDYN 2019 7th ECCOMAS Thematic Conference on Computational Methods in Structural Dynamics and Earthquake Engineering*, Crete; Greece; 24th-26th June 2019: 2019.

16. De Falco A, Giresini L, Sassu M. {T}emporary preventive seismic reinforcements on historic churches: numerical modeling of {S}an {F}rediano in {P}isa. *Applied Mechanics and Materials* 2013; **351**–**352**: 1393–1396.

17. Alecci V, De Stefano M. Building irregularity issues and architectural design in seismic areas. *Frattura Ed Integrità Strutturale* 2019; **13**(47): 161–168.

18. Giresini L, Taddei F, Casapulla C, Mueller G. Stochastic assessment of rocking masonry façades under real seismic records. *COMPDYN 2019 7th ECCOMAS Thematic Conference on Computational Methods in Structural Dynamics and Earthquake Engineering*, Crete; Greece; 24th-26th June 2019: 2019.

19. Casapulla C, Maione A, Argiento LU, Speranza E. Corner failure in masonry buildings: An updated macro-modeling approach with frictional resistances. *European Journal of Mechanics, A/Solids* 2018; **70**. DOI: 10.1016/j.euromechsol.2018.03.003.

20. Casapulla C. On the resonance conditions of rigid rocking blocks. *International Journal of Engineering and Technology* 2015; **7**(2): 760–771.

21. Casapulla C., Maione A. Critical Response of Free-Standing Rocking Blocks to the Intense Phase of an Earthquake. *International Review of Civil Engineering* 2017; **8**(1).

22. Lallemant D, Kiremidjian A, Burton H. Statistical procedures for developing earthquake damage fragility curves. *Earthquake Engineering & Structural Dynamics* 2015; **44**(9): 1373–1389. DOI: 10.1002/eqe.2522.

23. Stochino F, Attoli A, Concu G. Fragility Curves for RC Structure under Blast Load Considering the Influence of Seismic Demand. *Applied Sciences* 2020; **10**(2): 445.

24. Froli M, Giresini L, Laccone F. Dynamics of a new seismic isolation device based on tribological smooth rocking (TROCKSISD). *Engineering Structures* 2019; **193**: 154–169.

25. Froli M, Giresini L, Laccone F. A new seismic isolation device based on tribological smooth rocking (TRockSISD). *7th International Conference on Computational Methods in Structural Dynamics and Earthquake Engineering, COMPDYN 2019*, Crete; Greece; 24 June 2019 through 26 June 2019: 2019.

26. MATLAB. version 9.4.0.813654 (R2018a). The MathWorks Inc., Natick, Massachusetts, 2018.

27. Giresini L, Sassu M, Sorrentino L. In situ free-vibration tests on unrestrained and restrained rocking masonry walls. *Earthquake Engineering & Structural Dynamics* 2018; **47**(15): 3006–3025. DOI: 10.1002/eqe.3119.